Traceable determination of the size of nanoparticles up to 500 nm by scanning electron microscopy in transmission mode based on simulation

OPEN ACCESS
IOP Publishing
Measurement Science and Technology
Meas. Sci. Technol. **34** (2023) 085016 (10pp)
https://doi.org/10.1088/1361-6501/acd078

Traceable determination of the size of nanoparticles up to 500 nm by scanning electron microscopy in transmission mode based on simulation

Dorothee Hüser, Detlef Bergmann and Tobias Klein*

Physikalisch-Technische Bundesanstalt, Bundesallee 100, 38116 Braunschweig, Germany

E-mail: tobias.klein@ptb.de

Received 19 January 2023, revised 21 April 2023
Accepted for publication 26 April 2023
Published 22 May 2023

Abstract

The size measurement of nanoparticles contributes to the understanding of their properties and, thus, to the assessment of the risks they pose to health and the environment. For such measurements to be comparable and legally recognized, they must be traceable to the SI unit meter. Recently, interest in traceable measurements of polystyrene particles with sizes up to 500 nm has aroused, e.g. in the aerosol community. To meet this demand, we adapted an established method to traceably measure nanoparticles with high precision in the transmission mode of a scanning electron microscope (STEM-in-SEM or TSEM). Since this method was geared towards smaller particles, we adapted it at two points: New simulations with the program Geant4SEM allow a more accurate modelling, especially of the inelastical scattering processes. In addition, the image evaluation procedure was revised to account for the non-linear signal response at the particle boundary. The measured values obtained in this manner show good agreement with the values of two international intercomparisons.

Keywords: nanoparticle, nanoparticle size, STEM-in-SEM, TSEM, Monte Carlo simulation, Geant4SEM, Geant4

(Some figures may appear in colour only in the online journal)

1. Introduction

The field of nanotechnology demands quantitative assessment procedures of the features of nanoparticles. The characterization of mechanical and chemical material properties in conjunction with geometrical properties such as size and shape is relevant in particular for security reasons concerning health care [1], food safety, environmental issues such as pollution [2], and alike. In 2018, Warheit provided an overview [3] of projects and activities to understand the potential hazards associated with exposure to new materials, whether in medical, cosmetic or industrial applications. In 2017, Rauscher *et al* have published a survey on the *Regulatory Aspects of Nanomaterials in the European Union* [4]. Diverse research efforts are ongoing [5–8], in particular metrological strategies to quantify properties traced to the SI units, since such measurements are mandatory for measurements related to the EU definition of nanomaterials [9] and thus often accomplished by national metrology institutes [10–12] which conduct international comparisons to validate their

* Author to whom any correspondence should be addressed.

methods [13–15]. One goal of the metrological determination of size distributions of nanoparticles is to provide physical measurement standards to characterize particle measurement instruments.

To meet this demand we have developed a traceable measurement method for nanoparticles with sizes up to 200 nm already some time ago based on scanning electron microscopy in transmission mode (STEM-in-SEM or TESM) and an automated image analysis using the results of Monte Carlo simulations [10]. Its high accuracy could be demonstrated by participating in two international intercomparisons [13, 15]. The method is also used to provide the traceability for the measurements of the working group 'Aerosol and Particle Measurements' of the German metrology institute PTB [16] which aims to make aerosol measurements more comparable [17], especially for the automotive industry [18], e.g. by performing type approval tests for particle number counters. To this end, a calibration facility for reference particle number counters has been developed, which involves a differential mobility analyser (DMA) to measure the counting efficiency and linearity related to electrical mobility diameters. The traceability route for DMAs is described in ISO 15900:2020, which demands for size measurement of reference nanoparticles with uncertainties below 5% [19].

Thus, there is a demand for traceable size measurements of larger polystyrene particles, which are particularly popular in the aerosol community. Larger polystyrene particles pose a number of challenges compared to metal or smaller polystyrene particles, which will be discussed in the course of this paper. Eventually, these challenges can be overcome by enhanced Monte Carlo simulations that take into account individual inelastic scattering events and by a revised image analysis routine tailored to the properties of large latex particles.

In the next section, the measurement method and instrumentation, which remains the same as detailed in [10] and [20], is summarized and the aspect of calibrating the scanning field of the SEM, i.e. its pixel size, is pointed out. Section 3 explains the physical model used for the new Monte Carlo simulation. In section 4 the modified version of the image analysis routine, that is used to determine the diameter of spherical nanoparticles, is presented. Finally, the results of the proposed method are presented and discussed in section 5.

2. Measurement method

The signal of the bright field detector of a scanning electron microscope operated in transmission mode was used to image the nanoparticles [10]. The present work addresses spherical nanoparticles, in particular polystyrene particles, in the size range of 200 nm–500 nm, which have not been considered before. They are produced 'bottom up' by wet chemical synthesis, and are usually delivered in liquid suspension. The samples were prepared by depositing the particles on typical TEM grids, which consist of a thin carbon film supported by a nickel or copper grid, a process that is described in more detail in section 2.3 of [10].

A Zeiss LEO Supra 35VP scanning electron microscope was operated in the transmission mode with an electron beam energy of 30 keV. The beam spot size (Airy disk diameter) was estimated to be approximately in the range of 3 nm–6 nm (full width at half maximum, FWHM) at its focal plane. The divergence was estimated to be a half-cone angle of approximately 5.3 mrad.

The transmission detector consists of five solid-state electron detectors, four of which are used as dark field detectors. The bright field detector is mounted beneath a square aperture with an edge length of 140 µm corresponding to an average aperture of 16 mrad if the distance between the sample and the bright field detector is adjusted to 5 mm. This distance was used for all measurements presented in this article.

To realize traceability, the lateral scales defining the pixel size for each planar axis and their deviations from scan linearity have been characterized by measuring calibrated grids as physical measurement standards. Klein *et al* [10, 21] describe the details of the measurement process and the contributions to the overall measurement uncertainty. Edge distortions of the scanning system were avoided by omitting sufficiently large regions at the turning points. The physical measurement standards were calibrated at PTB using a laser diffractometer similar to the procedure described in [22].

The gray-scale values stored as tif images are proportional to the transmission yield values and do not need to be calibrated for the subsequent processing method.

3. Monte Carlo simulation using Geant4SEM

In 2018, Walker *et al* [23] investigated and compared various simulation programs. They revealed that the transmission signal obtained by Monte Carlo programs using the so-called continuous slowing down approximation (CSDA) for inelastic scattering resembles a model without any inelastic processes. In CSDA, the energy loss of the primary electrons is determined for a given path, but the angular deflection due to inelastic scattering processes is neglected. The Monte Carlo software which we have used up to now, MCSEM, also utilizes this rather simple inelastic model [10]. Therefore, we implemented a more realistic model for electron scattering using the powerful open-source Monte Carlo framework GEANT4 [24], which already has been used for similar purposes [25].

GEANT4 has been developed by a large consortium originating from high-energy physics, and has thus been designed to simulate high-energy projectile particles propagating through large or even huge macroscopic components of material. Consequently, modelling discrete scattering events would consume too much computation time and is thus avoided by so-called condensed history approaches [26]. Although some recent work to overcome this shortcoming has been carried out in the framework of the Geant4-DNA project [27], we decided to go for a home-made solution called Geant4SEM implementing discrete single scattering processes.

The simulation of the electron microscope uses a beam width of 5 nm (FWHM), a divergence angle of the beam of 5.3 mrad and a primary electron energy of 30 keV. The

detection system was simulated with a distance of 5 mm between the nanoparticles and the sensitive rectangular detection area of 140 µm × 140 µm.

The nanoparticles are modelled as homogeneous solids with discrete point-like scatter centres, which are randomly distributed, neglecting any molecular or crystalline structures (jellium model). The trajectory of a probe electron is built as a sequence of straight path segments and vertices, where the vertices represent the positions of the scatter events. The specific length s of a path is calculated as a function of a uniformly distributed random number $R \in [0,1)$ and the mean free path λ

$$s = -\lambda \log(R). \tag{1}$$

In each step, the potential elastic and inelastic path lengths for each chemical element present in the compound are determined using independent random numbers R. Subsequently, the scattering event with the shortest individual path length is chosen and modelled, and the differential cross-section of the actual interaction type is used to determine the change in propagation direction as well as the energy loss E_{loss} of the probe electron in the case of inelastic scattering.

The (double) differential cross-sections represent the probability density distributions p

$$\text{elastic}\colon\ p(\theta) \propto \frac{\mathrm{d}\sigma}{\mathrm{d}\Omega} \tag{2}$$

$$\text{inelastic}\colon\ p(E_{\mathrm{loss}}, q(\theta)) \propto \frac{\mathrm{d}\sigma}{\mathrm{d}E_{\mathrm{loss}}\,\mathrm{d}q(\theta)} \tag{3}$$

with the solid angle $\mathrm{d}\Omega = \sin(\theta)\,\mathrm{d}\theta\,\mathrm{d}\varphi$, and $\theta = \arccos(\mathbf{e}_{\mathrm{in}} \cdot \mathbf{e}_{\mathrm{out}})$, where $\mathbf{e}$ is the unity vector of the momentum directions of the probe electron, and q is the magnitude of the momentum transfer. Therefore, θ denotes the polar angle of the outgoing momentum with respect to the incoming momentum. The angle $\varphi \in [0, 2\pi)$ is the uniformly distributed azimuth angle. Probability density distributions are normalized: $\int p(x)\mathrm{d}x = 1$.

The total and differential cross-sections of the elastic scattering processes were evaluated using ELSEPA [28] with finite-sized muffin tin radii to account for solids in contrast to free atoms. The mean free path of elastic interactions depends on the total cross-section and density of the atomic nuclei of a chemical element. Polysterene is modelled as C_8H_8 with muffin tin radii $r_{\mathrm{MT}} = 0.077\,\mathrm{nm}$ for carbon and $r_{\mathrm{MT}} = 0.037\,\mathrm{nm}$ for hydrogen. For the simulation, the value of the density ρ of polystyrene is set to $\rho = 1.05\,\frac{\mathrm{g}}{\mathrm{cm}^3}$.

3.1. Model of inelastic scattering

The probability distribution of the energy loss E_{loss} is the marginal distribution $p(E_{\mathrm{loss}}) = \int p(E_{\mathrm{loss}}, q(\theta))\,\mathrm{d}q$. The energy loss is determined according to a uniformly distributed random number $R \in [0,1)$ with

$$E_{\mathrm{loss}} = P_E^{-1}(R) \tag{4}$$

where P_E^{-1} is the inverse function of P_E and P_E is the cumulative function of $p(E_{\mathrm{loss}})$. Accordingly, in the case of inelastic scattering for a given E_{loss}, the polar angle θ is determined by dicing a random number $R \in [0,1)$

$$\theta = P_\theta^{-1}(R) \tag{5}$$

where P_θ is the cumulative function of $p(\theta)$, resp. $p(E_{\mathrm{loss}}, q(\theta))$.

The model of inelastic scattering is far more detailed than the continuous slowing-down approximation, treating single scatter events with appropriate angular deflections. However, it is still considerably simplified compared to the full dielectric function theory approaches and *ab initio* density functional theory for calculating excitations. It phenomenologically considers excitations as oscillators. Plasmon oscillations are expressed as in equation (7) in [29], and excitations of shell electrons are modelled as oscillators with characteristic resonances at energies E_i with peak widths γ_i that are related to their relaxation times, approximating equation (1a) of [30].

The mean free path λ_{inel} is the inverse of the scatter rate τ: $\lambda_{\mathrm{inel}} = \frac{1}{\tau}$. The rate of inelastic scattering events is determined by

$$\tau = \int_{E_{\mathrm{loss,min}}}^{E_{\mathrm{loss,max}}} \frac{\mathrm{d}\sigma}{\mathrm{d}E_{\mathrm{loss}}}\,\mathrm{d}E_{\mathrm{loss}}. \tag{6}$$

The energy loss is determined using its probability density distribution $p(E_{\mathrm{loss}})$, which is proportional to the differential cross-section:

$$\frac{\mathrm{d}\sigma}{\mathrm{d}E_{\mathrm{loss}}} = \int_{q_-}^{q_+} \frac{\mathrm{d}\sigma}{\mathrm{d}q\,\mathrm{d}E_{\mathrm{loss}}}\,\mathrm{d}q \tag{7}$$

with

$$q_\pm = \sqrt{2}\left(\sqrt{E_{\mathrm{kin}}} \pm \sqrt{E_{\mathrm{kin}} - E_{\mathrm{loss}}}\right) \tag{8}$$

and with the double differential cross-section being modelled as

$$\frac{\mathrm{d}\sigma}{\mathrm{d}q\,\mathrm{d}E_{\mathrm{loss}}} = \frac{1}{\pi\, a_0 E_{\mathrm{kin}} q} \sum_{i=1}^{n} \frac{A_i\, E_{\mathrm{loss}}\, \gamma_{i,q}}{\left(E_{i,q}^2 - E_{\mathrm{loss}}^2\right)^2 + \left(E_{\mathrm{loss}}\,\gamma_{i,q}\right)^2} \tag{9}$$

where a_0 is the Bohr radius and A_i are weights for relative peak heights. The peak widths $\gamma_{i,q}$ and resonance energies $E_{i,q}$ are modelled as

$$\gamma_{i,q} = \gamma_i + c_0 q + c_1 q^2 \tag{10}$$

and

$$E_{i,q} = E_i + c_2 q + c_3 q^2, \tag{11}$$

respectively.

Table 1. Parameters of equations (10) and (11) for polystyrene.

c_0	c_1	c_2	c_3
20	250	0	0.5

Table 2. Parameters of equation (9) for polystyrene with three resonances ($n = 3$).

i	E_i (eV)	γ_i (eV)	A_i
1	7	1.5	3
2	22	9	260
3	300	100	50

The angle θ between the directions of a probe electron before and after an inelastic scattering process is derived from the double differential cross-section, as shown in equation (9), using

$$q = \sqrt{4E_{\mathrm{kin}} - 2E_{\mathrm{loss}} - 4\sqrt{E_{\mathrm{kin}}}\sqrt{E_{\mathrm{kin}} - E_{\mathrm{loss}}}\cos(\theta)}. \quad (12)$$

The parameters for polystyrene, with three resonances ($n = 3$), were obtained by fitting them in a way that data from literature could be approximately reproduced: figures 2, 3, 6, and table I of [31], as well as figure 1 in [32], and in particular the K-shell excitation at $E_3 = 300\,\mathrm{eV}$ in figure 1 of [33]. The values of all the parameters are listed in tables 1 and 2.

The simulation was performed using the tracking and stepping engine of GEANT4. The electron scattering model was implemented in two different concrete classes for elastic and inelastic scattering which were derived from the abstract GEANT4 class `G4VDiscreteProcess` to realize single scattering events. The nanoparticle and the bright field transmission detector were included as a derived class from the abstract GEANT4 class `G4VUserDetectorConstruction`. The probe electron beam was simulated with a concrete class derived from the abstract GEANT4 class `G4VUserPrimaryGeneratorAction`.

4. Image analysis

A large number of particles is required to obtain statistically reliable results. We have developed a software that automatically analyses bright-field STEM-in-SEM images to process several thousand particles as detailed in section 4 of [10]. Figure 1 shows an example of a micrograph of a sample of spherical polystyrene nanoparticles with a nominal size of 500 nm. Several hundred micrographs were acquired to collect sufficient particles for statistical analysis.

The software was written in MATLAB [34], incorporating routines from ImageJ [35]. The micrographs are preprocessed before an individual analysis of each particle is performed. A global threshold value according to Otsu [36] is used to provisionally segment the background and foreground pixels. Afterwards, 'objects' which could potentially be particles are located and subsequently individually treated to determine their size, as described in the following subsections. After this treatment, artifacts originating e.g. from inhomogeneous carbon films or drying residues are distinguished from particles based on their size and circularity.

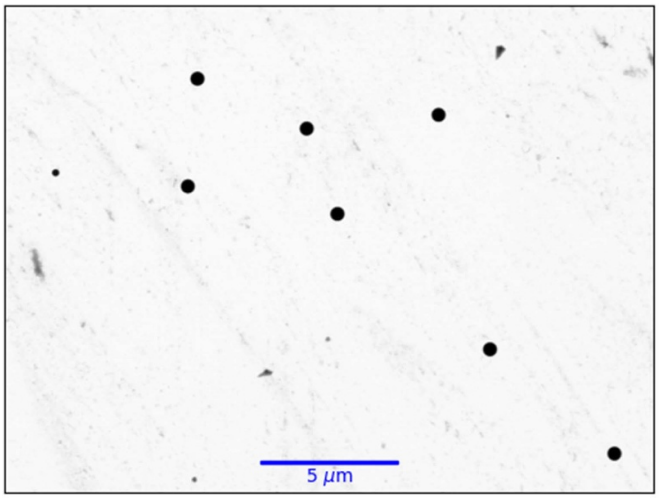

Figure 1. One of several hundred STEM-in-SEM bright field micrographs of a sample of spherical polystyrene nanoparticles with a nominal size of 500 nm.

4.1. Thresholding

While Gontard *et al* [37] used a regular grid of sub-images with local thresholds per sub-image and noise reduction, we process each particle with its individual gray value threshold at the boundary g_{bd} dependent not only on the specific microscope settings but also on the size of the particle and its material [10].

$$g_{\mathrm{bd}} = \underbrace{\frac{S_{\mathrm{bd}} - S_0}{S_1 - S_0}}_{=:t_{\mathrm{rel}}} (g_1 - g_0) + g_0 \quad (13)$$

S_{bd} is the *simulated* transmission yield at the particle boundary, S_1 is the *simulated* transmission yield on the support film, and S_0 is the *simulated* transmission yield on the pole of the particle, that is the minimum intensity at the centre of the particle because the images are bright-field signals. Accordingly, g_1 and g_0 are the gray values of the support film and at the centre of the particle, respectively. The ratio t_{rel} is the *relative threshold*.

The principal idea of our procedure to determine the diameter of spherical nanoparticles is to be independent of any calibration of the gray-scale of the bright field detector signal and to be independent of the knowledge of the characteristics of the support film. This works out because the ratio of the gray value differences in the measurement is equal to the ratio of the simulated differences in the transmission yield. Equation (13) can be rewritten as follows, illustrating this clearly

$$t_{\mathrm{rel}} = \frac{S_{\mathrm{bd}} - S_0}{S_1 - S_0} = \frac{g_{\mathrm{bd}} - g_0}{g_1 - g_0}. \quad (14)$$

The size of each particle is determined by counting the number of pixels m below a certain threshold $g_{\mathrm{thr}} = g_{\mathrm{bd}}$. The

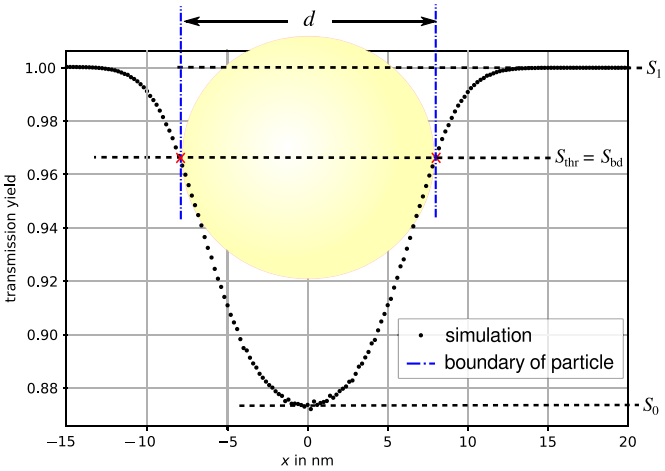

Figure 2. Using the threshold value at the particle boundary ($S_{thr} = S_{bd}$) is valid if the transmission yield signal is linear in the vicinity of the boundary as is shown here for a polystyrene particle of $d_{bd} = 16\,nm$.

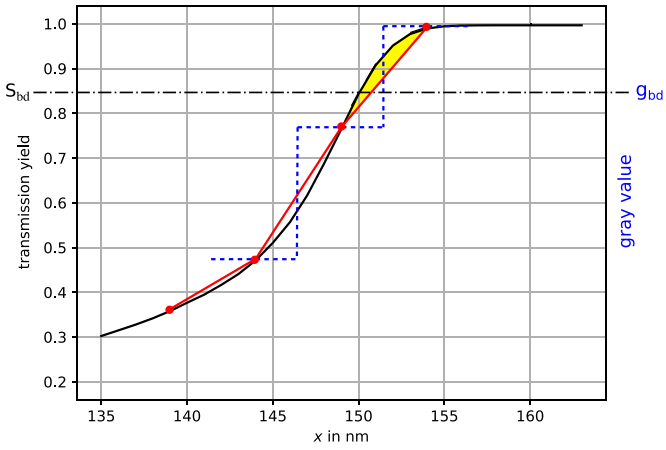

Figure 3. For this polystyrene particle with $d_{bd} = 300\,nm$, using $S_{thr} = S_{bd}$ would lead to an overestimation of its size due to the linear interpolation (red) between pixels (blue) with finite pixel resolution despite the curvature of the yield curve (black) at the particle boundary.

subscript 'thr' denotes 'threshold' and 'bd' denotes 'boundary'. Each pixel has a rectangular area $a = p_x p_y$, which is the product of the pixel sizes p_x and p_y in the x- and y-direction, respectively, which were calibrated using the two-dimensional grid standard mentioned previously. The bright-field image delivers a projection of the sphere, that is a circular disk with varying gray values. We approximate the area of the projection of one particle i by the total area A_i of all the pixels with gray values below the threshold $g_{thr,i}$ assigned to the ith particle. The indices i are the identifying enumeration indices for the particles $i = 1,\ldots,N$ where N is the number of measured particles. With m_i being the number of pixels with gray values below $g_{thr,i}$ the area is

$$A_i = a m_i. \tag{15}$$

The diameter of the single particle under consideration, which is assumed to be spherical, is derived from area A_i as

$$d_i = 2\sqrt{\frac{A_i}{\pi}}. \tag{16}$$

In case of particles like silver or gold with relative yields $t_{rel} = \frac{S_{bd}-S_0}{S_1-S_0}$ in the range of 0.5–0.7, the threshold value is chosen to be the boundary gray value $g_{thr} = g_{bd}$ and is calculated iteratively because it depends on the size of the particle [10]. The final size of the particle is subsequently determined in a linearly interpolated image to achieve subpixel accuracy. This approach is valid if the signal profile in the vicinity of at least two pixels around g_{bd} is linear, as shown in figure 2.

However, polystyrene is a low-density and low-atomic-number material, and thus the transmission yield rises rapidly at the vicinity of the particle's boundary and reaches values close to one. Figure 3 shows that the slope of the transmission yield changes drastically within a pixel, and thus, the prerequisite of a linear variation of gray values along neighbouring pixels is no longer fulfilled. This especially affects the measurement of larger particles, for which larger pixel sizes are chosen, making the interpolation prone to errors.

To overcome these problems, a fixed relative threshold t_{rel} is chosen to determine a preliminary value that is subsequently adjusted to obtain the final particle size.

This approach also solves another issue, which is particularly pronounced for large particles. Surfactants that are needed to stabilize the suspension of particles in liquid tend to concentrate in the cavity underneath the spherical particles during sample preparation and drying. Thus, the larger the particle, the more surfactant, and the lighter the particles the greater its impact, especially close to the particle's boundary, which hinders the distinction of background and foreground pixels.

4.2. Determination of diameter based on simulation

For the polystyrene particles, we chose a relative threshold of $t_{rel} = 0.6$, and consequently, a threshold gray value of

$$g_{thr} = 0.6\,(g_1 - g_0) + g_0 \tag{17}$$

which leads to smaller particle areas, requiring a subsequent adjustment of the size with the aid of the simulated yield values. The simulation effort is comparable to that of the established approach, and the analysis effort for thousands of particles is even smaller because the iteration over the size is no longer needed. After a size is determined by applying g_{thr} to obtain a preliminary area and thus a preliminary diameter, the size adjustment is looked up from tabulated values obtained by simulation.

The diameter d_{rel} derived from the area covered by the pixels below

$$S_{thr} = 0.6\,(S_1 - S_0) + S_0 \tag{18}$$

is compared with the 'real' diameter of the sphere d_{bd}. The differences $\Delta = d_{bd} - d_{rel}$ are tabulated as a function of d_{rel}.

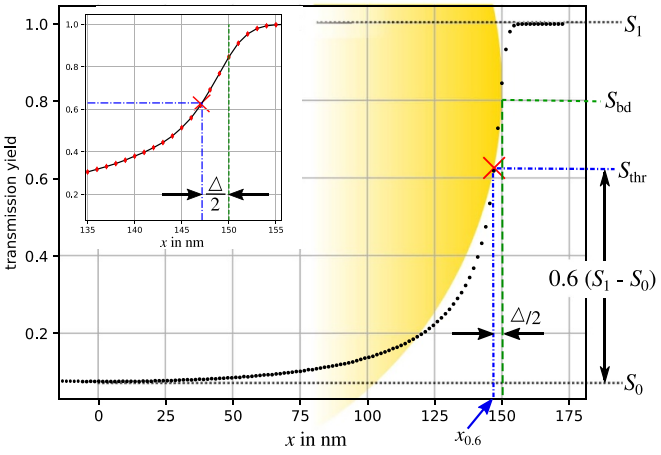

Figure 4. The transmission yield along the meridian of a polystyrene sphere with $d_{bd} = 300\,\text{nm}$ is shown as an example. At the constant threshold $S_{thr} = 0.6\,(S_1 - S_0) + S_0$ a diameter $d_{0.6} = 2x_{0.6} = 294.3\,\text{nm}$ is determined to be tabulated together with the adjustment term $\Delta = d_{bd} - d_{0.6} = 5.7\,\text{nm}$.

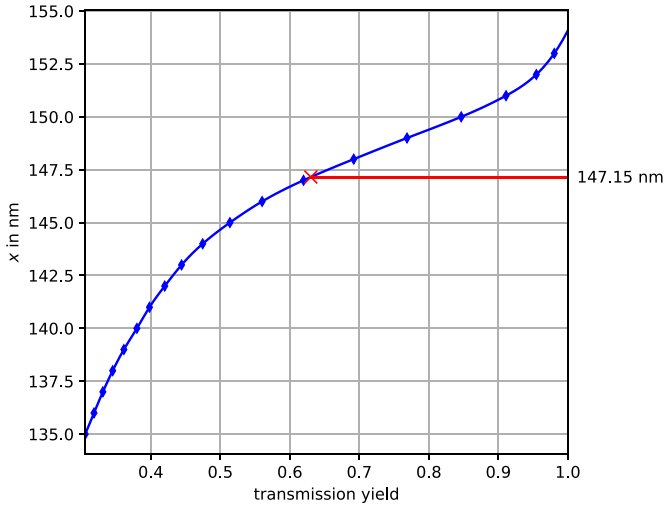

Figure 5. Inverse function of the transmission yield distribution along the positive part of the meridian of a polystyrene sphere in the vicinity of the constant threshold of 60%.

Figure 4 shows the idea behind the method to determine the diameter d_{rel} for a fixed predefined relative threshold of $t_{rel} = 0.6$. Each entry pair $(d_{0.6}, \Delta)$ of the lookup table is obtained by simulating the transmission yield function S which defines the transmission yield dependent on the lateral position x, with the origin $x = 0$ at the pole

$$S : x \mapsto S(x) \tag{19}$$

and a segment along the meridian of a sphere of specified diameter d_{bd}, that lies in the vicinity of the 60%.

During simulation, the support film is neglected such that $S_1 = 1$ which is equivalent to the common assumption of a homogenous support film. The simulated transmission yield value of a sphere centred at $x = 0$ at the pole is $S_0 = S(0)$.

Position x_{rel} is evaluated by the inverse function of the transmission yield distributions along the positive part of the meridian in the vicinity of 60%:

$$x_{rel} = S^{-1}(S_{thr}) = S^{-1}\left(t_{rel}(1 - S_0) + S_0\right). \tag{20}$$

The discrete positions of the simulated pairs of values $(S^{-1}(S_{thr}), x_{rel})$ are interpolated using a cubic spline. As an example, figure 5 shows the inverse function of equation (20) in the vicinity of the 60% being interpolated by a cubic spline to determine $x_{0.6} = S^{-1}(S_{thr})$, with $S_0 = 0.0756$ such that $S_{thr} = 0.6303$ and finally $x_{0.6} = 147.15\,\text{nm} = S^{-1}(0.6303)$, i.e. the preliminary diameter is $d_{rel} = d_{0.6} = 2 \cdot 147.15\,\text{nm} = 294.3\,\text{nm}$.

The lookup table contains the values of $d_{rel} = 2x_{rel}$ and the corresponding Δ. It is used to adjust the value d_{rel} of each particle to obtain the sphere diameter d_{bd}. The resolution of the table is chosen in a way that allows for linear interpolation between the sampling points.

5. Results and discussion

Polysterene particles of nominally 500 nm, 300 nm and 200 nm, called PSL500, PSL300 and PSL200, respectively, were measured and evaluated using the revised method described previously. Table 3 shows the measurement results, together with the reference values and E_n values, which will be introduced shortly. Figure 6 depicts the deviation from the reference value in comparison to the uncertainty while the size distributions of all three samples are shown in figure 7.

The sample PSL500 with polystyrene particles of a nominal size of 500 nm was produced by Thermo Fisher Scientific as 'nanosphere size standard 3500A'. The manufacturer states a mean diameter of $510\,\text{nm} \pm 7\,\text{nm}$, [38] in accordance with our result of 512 nm. The histogram in figure 7 reveals the presence of a few particles that are considerably smaller, which holds for all the samples.

The samples PSL300 and PSL200 were chosen because they have already been measured in the framework of two interlaboratory comparisons and thus reliable information regarding their properties is available. The sample PSL300 was investigated during the APMP.L-S5 Supplementary Comparison on Nanoparticle Size, where it has been named P5 [15]. It was manufactured by the JSR Cooperation. The sample PSL200 was produced by Thermo Fisher Scientific (at that time Duke Scientific) as 'nanosphere size standard 3200A'. It was chosen as one sample in the *pilot study* which was carried out by the consortium of the European project 'Traceable measurement of nanoparticle size' [13].

In the two interlaboratory comparisons, nanoparticles were studied by a large number of metrology institutes using ensemble methods such as dynamic light scattering, differential mobility analysis, and small-angle x-ray scattering, as well as methods for analysing single particles (from approximately one hundred to some thousands in the case of STEM-in-SEM): besides STEM-in-SEM, traditional scanning electron

Table 3. Measurement results for polystyrene particles with sizes between 200 nm and 500 nm using the revised method show good agreement with reference values and small E_n values.

Reference values			Revised method				Established method	
d_r (nm)	U_r (nm)	Reference	d (nm)	U (nm)	Pixel size (nm)	E_n	d_{est} (nm)	E_n
510	7	[38]	512	12	23.0	0.13	not evaluated	
305.73	1.18	[15]	306.9	7.2	19.1	0.16	not reported	
197.68	4.54	[13]	197.0	4.1	4.5	0.11	201.0	0.37

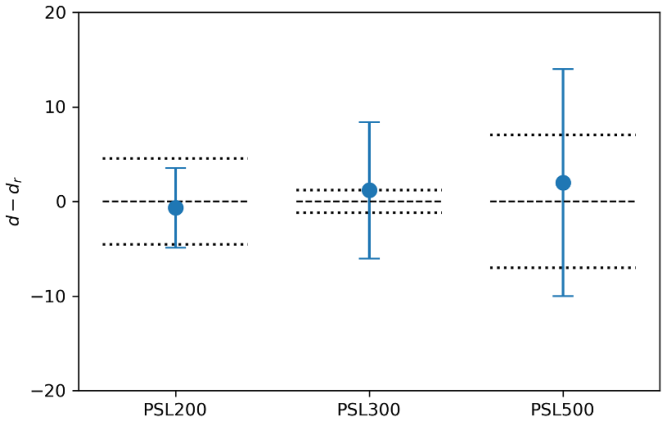

Figure 6. Deviation from reference diameter d_r in comparison to the uncertainties of both the reference diameter and the measurement result.

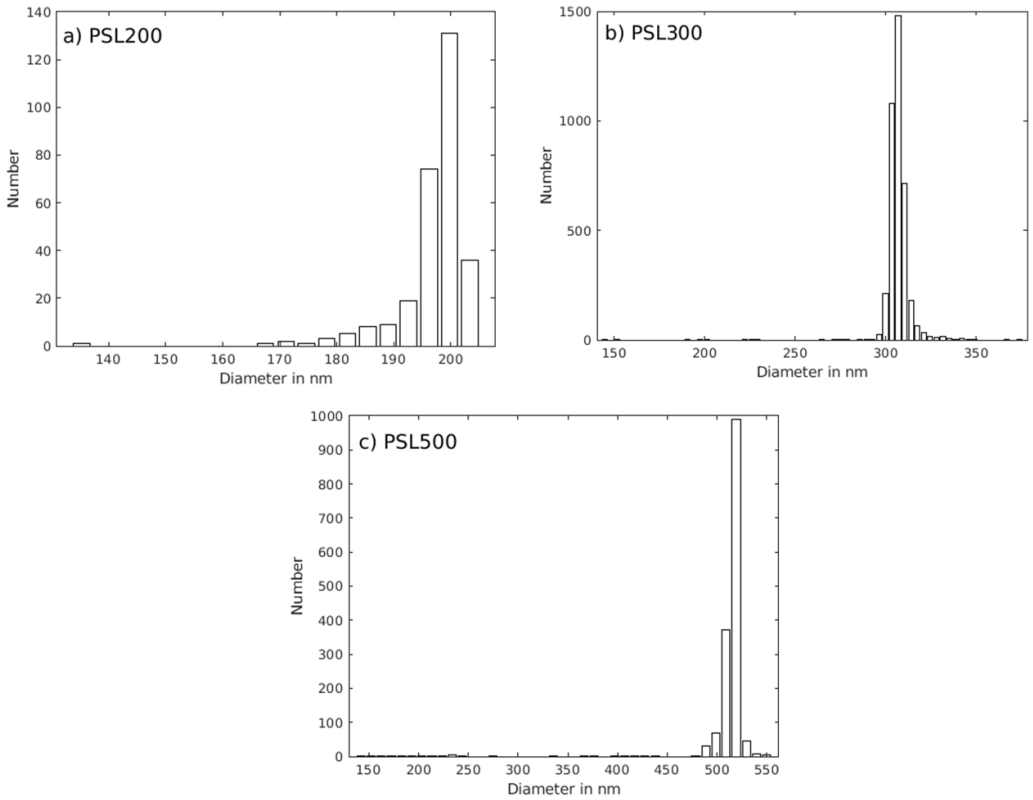

Figure 7. Size distributions of PSL200 (a), PSL300 (b) and PSL500 (c).

microscopy using the secondary electron signal (SEM), transmission electron microscopy (TEM), and atomic force microscopy have been used.

The international comparisons confirmed a good consistency of the results achieved with our established method for particles with sizes up to 200 nm. Although we also took STEM-in-SEM micrographs of PSL300, we did not report any value because of the apparent issues discussed in this paper, which had not been resolved at that time.

The data contributed by the large number of metrology institutes and the various measurement and analysis methods for the international comparisons were compared using t-tests that are formulated as E_n-tests. The t-test compares the mean values $\bar{d}_1$ and $\bar{d}_2$ of two samples by weighting their difference with the Pythagorean sum $\sqrt{\bar{s}_1 + \bar{s}_2}$ of the standard deviations of the means $\bar{s}_1$ and $\bar{s}_2$. To avoid issues with the question of the number of degrees of freedom to determine a common quantile t (in metrology referred to as expansion factor k), the test quantity is redefined such that the quantile t is included in the standard deviations of the means. The standard deviation of the mean $\bar{s}_l$ of each of n participating laboratories $l = 1, \ldots, n$ is replaced by the expanded uncertainty $U_l = t\bar{s}_l$. For an interlaboratory test, sample 1 is each of the participants' results $l = 1, \ldots, n$ and sample 2 is a reference r with $\bar{d}_l$, $\bar{d}_\mathrm{r}$, U_l, and U_r.

The hypothesis that $\bar{d}_l$ and $\bar{d}_\mathrm{r}$ agree is accepted if

$$\frac{|\,\bar{d}_l - \bar{d}_\mathrm{r}\,|}{\sqrt{\bar{s}_l + \bar{s}_\mathrm{r}}} < t \quad \Rightarrow \quad E_\mathrm{n} = \frac{|\,\bar{d}_l - \bar{d}_\mathrm{r}\,|}{\sqrt{U_l + U_\mathrm{r}}} < 1. \tag{21}$$

Furthermore, in the absence of a reference value that is superior to any other value of the participating laboratories, Cox [39] has modified the test quantity by using the weighted sum of all values $\bar{d}_l$ under test as the reference $\bar{d}_\mathrm{r}$, dependent on all $\bar{d}_l$ and all uncertainties $U_l = tu_l$. The uncertainty of the reference $U_\mathrm{r} = tu_\mathrm{r}$ is obtained by summing the inverse (eventually expanded) uncertainties

$$u_\mathrm{r} = \left(\sum_{l=1}^{n} \frac{1}{u_l^2} \right)^{-\frac{1}{2}} \tag{22}$$

$$\bar{d}_\mathrm{r} = \sum_{l=1}^{n} w_l \bar{d}_l \quad \text{with} \quad w_l = \frac{u_\mathrm{r}^2}{u_l^2}. \tag{23}$$

The test quantity [39] then changes to

$$E_\mathrm{n} = \frac{|\,\bar{d}_l - \bar{d}_\mathrm{r}\,|}{\sqrt{U_l - U_\mathrm{r}}} < 1. \tag{24}$$

The test quantity for the newly evaluated results is independent of $\bar{d}_\mathrm{r}$ of the reference, such that the E_n used to assess the new results is that of equation (21).

The E_n values shown in table 3 were calculated using the original reference values of the intercomparisons that were unaffected by our new results. Nevertheless, the achieved E_n values are unexpectedly small, with values in the order of 0.1. This indicates a very good agreement between the measurement results of the revised method and the original reference values also in the cases of larger particles that could not be correctly measured using the established method. On the other hand, even for the smallest sample PSL200, the agreement is better (and thus the E_n value is smaller) compared to result of the established method.

A re-evaluation of the micrographs of the smaller particles with sizes down to 30 nm used in the intercomparisons with the revised method revealed only slight changes in the results, which are thus compliant with both the results of the established method and the reference values of the intercomparisons.

Such small E_n values, as listed in table 3, generally raise the question whether the corresponding uncertainties could have been overestimated. However, while the uncertainties of approximately 2.5% effortlessly satisfy the requirement for DMA calibration as defined by ISO 15900:2020 [19] and discussed in the Introduction, they lie in the same range as those of the established method. The smaller E_n values result from better agreement with the reference value and not from significantly enlarged uncertainties. In addition, the uncertainties for the large particles are hardly larger than half a pixel size, so their further reduction seems questionable.

Although this method has been developed for reference materials which typically have smooth surfaces, we expect that it will also be advantageous for the measurement of particles from environmental samples, which often have rough surface structures due to attached organic and chemical substances. On the one hand, the TSEM signal is less disturbed by these substances compared to secondary electron signals. On the other hand, the evaluation of the particle size at a fixed threshold 'inside' the particle makes the method robust to disturbances at the particle boundary.

6. Conclusion and outlook

By introducing two enhancements to our established method for highly accurate, traceable size measurement of nanoparticles, its applicability could be extended to larger particles with sizes of up to 500 nm, which are of low density, such as polystyrene. On the one hand, the Monte Carlo simulation of the image formation process has been complemented with a model for individual inelastic scattering events including angular deflection. On the other hand, the image analysis process has been revised in order to address particles with nonlinear signal profiles close to their boundary. To this end, a preliminary size is determined at the linear portion of the signal profile, followed by an adjustment of the size based on the simulation results. The measurement results of the revised method agree with reference values from two intercomparisons, while at the same time expanding the applicability to larger particles and providing even more accurate results in the intermediate size range.

While we only tested the revised method for particles with sizes up to 500 nm, we are confident that it will also work for even larger particles as long as the larger pixel sizes will be considered, e.g. in the determination of measurement uncertainty. We anticipate that the revised method,

especially the enhanced simulations, may also lead to accurate thickness measurements, which have been shown to depend on the choice of the physical model used in the simulation [40]. Since STEM-in-SEM measurements of spherical nanoparticles spanning the size range of up to 500 nm are now possible, the next step would be traceable measurements of non-spherical nanoparticles.

Data availability statement

The data cannot be made publicly available upon publication because the cost of preparing, depositing and hosting the data would be prohibitive within the terms of this research project. The data that support the findings of this study are available upon reasonable request from the authors.

Acknowledgment

The authors wish to thank John Villarrubia for highly appreciated discussions on the treatment of inelastic scattering in Monte Carlo simulations and they are grateful to Egbert Buhr, who contributed fundamental ideas and continued discussions.

ORCID iDs

Dorothee Hüser https://orcid.org/0000-0002-2208-4490
Tobias Klein https://orcid.org/0000-0002-3875-6095

References

[1] Möhlmann C, Schumacher C, Gasse B, Plitzko S and Broßell D 2021 Grouping of exposure and risk for processing of nanocomposites *J. Phys.: Conf. Ser.* **1953** 012006
[2] Andres H *et al* 2014 Measuring soot particles from automotive exhaust emissions *EPJ Web Conf.* **77** 00020
[3] Warheit D B 2018 Hazard and risk assessment strategies for nanoparticle exposures: How far have we come in the past 10 years? *F1000Research* **7** 379
[4] Rauscher H, Rasmussen K and Sokull-Klüttgen B 2017 Regulatory aspects of nanomaterials in the EU *Chem. Ing. Tech.* **89** 224–31
[5] Hörenz C Tache O, Bartczack D, Nunez S, Alvaro I A, Goenaga-Infante H and Hodoroaba V-D 2020 A study on the analysis of particle size distribution for bimodal model nanoparticles by electron microscopy *Microsc. Microanal.* **26** 2282–3
[6] Kim H, Han J and Han T Y-J 2020 Machine vision-driven automatic recognition of particle size and morphology in SEM images *Nanoscale* **12** 19461–9
[7] Usfoor Z, Kaufmann K, Rakib A S H, Hergenröder R and Shpacovitch V 2020 Features of sizing and enumeration of silica and polystyrene nanoparticles by nanoparticle tracking analysis (NTA) *Sensors* **20** 14
[8] Hodoroaba V-D , Hörenz C, Pellegrino F, Maurino V, Durand B and Taché O 2021 Nanoparticle size, shape and concentration measurement at once—two VAMAS pre-standardization projects ready to start *Microsc. Microanal.* **27** 2250–1
[9] European Union 2011 Commission Recommendation of 18 October 2011 on the definition of nanomaterial *Official J. Eur. Union* **L 275** 38–40
[10] Klein T, Buhr E, Johnsen K-P and Frase C G 2011 Traceable measurement of nanoparticle size using a scanning electron microscope in transmission mode (TSEM) *Meas. Sci. Technol.* **22** 9
[11] Yamamoto K and Fujimoto T 2014 Primary particle size distribution measurement of nanomaterials by using TEM *Microsc. Microanal.* **20** 1946–7
[12] Park B C and Kwak M J 2019 Investigation of digital imaging processing in determining nano-particle size distribution based on scanning electron microscopic image *Microsc. Microanal.* **25** 2654–5
[13] Meli F *et al* 2012 Traceable size determination of nanoparticles a comparison among European metrology institutes *Meas. Sci. Technol.* **23** 125005
[14] Takahashi K Kramar J A, Farkas N, Takahata K, Misumi I, Sugawara K, Gonda S and Ehara K 2019 Interlaboratory comparison of nanoparticle size measurements between NMIJ and NIST using two different types of dynamic light scattering instruments *Metrologia* **56** 055002
[15] Lin H-L *et al* 2019 Nanoparticle characterization—supplementary comparison on nanoparticle size *Metrologia* **56** 04004
[16] Kuntze A, Hildebrandt M, Nowak A, Jordan-Gerkens A, Bergmann D, Buhr E and Ebert V 2014 Characterization of a PTB-standard for particle number concentration of soot particles *18th ETH-Conf. on Combustion Generated Nanoparticles (Zurich, Switzerland)*
[17] Wiedensohler A *et al* 2018 Mobility particle size spectrometers: calibration procedures and measurement uncertainties *Aerosol Sci. Technol.* **52** 146–64
[18] Terres A, Giechaskiel B, Nowak A and Ebert V 2021 Calibration uncertainty of 23 nm engine exhaust condensation particle counters with soot generators: a European automotive laboratory comparison *Emiss. Control Sci. Technol.* **7** 124–36
[19] ISO 15900:2020 2020 *Determination of Particle Size Distribution—Differential Electrical Mobility Analysis for Aerosol Particles* (Geneva: International Organization for Standardization)
[20] Buhr E, Senftleben N, Klein T, Bergmann D, Gnieser D, Frase C G and Bosse H 2009 Characterization of nanoparticles by scanning electron microscopy in transmission mode *Meas. Sci. Technol.* **20** 084025
[21] Klein T, Buhr E and Frase C G 2012 TSEM: A review of scanning electron microscopy in transmission mode and its applications *Advances in Imaging and Electron Physics* vol 171, ed P W Hawkes (Amsterdam: Elsevier), ch 6 pp 297–356
[22] Buhr E, Michaelis W, Diener A and Mirande W 2007 Multi-wavelength VIS/UV optical diffractometer for high-accuracy calibration of nano-scale pitch standards *Meas. Sci. Technol.* **18** 667–74
[23] Walker C G H, Konvalina I, Mika F, Frank L and Müllerová I 2018 Quantitative comparison of simulated and measured signals in the STEM mode of a SEM *Nuclear Inst. Methods Phys. Res.* B **415** 17–24
[24] Agostinelli S *et al* (GEANT4-Collaboration) 2003 Geant4—a simulation toolkit *Nucl. Instrum. Methods Phys. Res.* A **506** 250–303
[25] Kieft E and Bosch E 2008 Refinement of Monte Carlo simulations of electron–specimen interaction in low-voltage SEM *J. Phys. D: Appl. Phys.* **41** 215310
[26] Kadri O, Ivanchenko V, Gharbi F and Trabelsi A 2009 Incorporation of the Goudsmit–Saunderson electron transport theory in the Geant4 Monte Carlo code *Nucl. Instrum. Methods Phys. Res.* B **267** 3624–32
[27] Sakata D *et al* 2018 Geant4-DNA track-structure simulations for gold nanoparticles: the importance of electron discrete models in nanometer volumes *Med. Phys.* **45** 2230–42

[28] Salvat F, Jablonski A and Powell C J 2005 and C J Powell. ELSEPA – Dirac partial-wave calculation of elastic scattering of electrons and positrons by atoms, positive ions and molecules *Comput. Phys. Commun.* **165** 157–90
[29] Ritchie R H and Howie A 1977 Electron excitation and the optical potential in electron microscopy *Phil. Mag.* **36** 463–81
[30] Fuentes G G, Elizalde E, Yubero F and Sanz J M 2002 Electron inelastic mean free path for Ti, TiC, TiN and TiO_2 as determined by quantitative reflection electron energy-loss spectroscopy *Surf. Interface Anal.* **33** 230–7
[31] Ashley J C, Tung C J and Ritchie R H 1978 Inelastic interactions of electrons with polysterene: calculations of mean free paths, stopping powers and CSDA ranges *IEEE Trans. Nucl. Sci.* **25** 1566–70
[32] Varlot K, Martin J M and Quet C 1998 Physical and chemical changes in polystyrene during electron irradiation using EELS in the TEM: contribution of the dielectric function *J. Microsc.* **191** 187–94
[33] Inagaki T, Arakawa E T, Hamm R N and Williams M W 1977 Optical properties of polysterene from near-infrared to x-ray region and convergence of optical sum rules *Phys. Rev.* B **15** 3243–53
[34] The MathWorks Inc. 2009 Matlab R2009a (available at: www.mathworks.com)
[35] Schneider C A, Rasband W S and Eliceiri K W 2012 NIH Image to ImageJ: 25 years of image analysis *Nature Methods* **9** 671–5
[36] Otsu N 1979 A threshold selection method from gray-level histograms *IEEE Trans. Syst. Man Cybern.* **9** 62–66
[37] Gontard L C, Ozkaya D and Dunin-Borkowski R E 2011 A simple algorithm for measuring particle size distributions on an uneven background from TEM images *Ultramicroscopy* **111** 101–6
[38] Thermo Fisher Scientific 2022 *Nanosphere Size Standards – Nist Traceable Diameter*
[39] Cox M G 2002 The evaluation of key comparison data *Metrologia* **39** 589–95
[40] Buhr E, Bug M U, Bergmann D and Cizmar P 2017 and C G Frase. Simultaneous measurement of lateral and vertical size of nanoparticles using transmission scanning electron microscopy (TSEM) *Meas. Sci. Technol.* **28** 034002